Eur. Phys. J. Spec. Top. (2026) 235:3577–3591
https://doi.org/10.1140/epjs/s11734-026-02357-0

THE EUROPEAN PHYSICAL JOURNAL SPECIAL TOPICS

Regular Article

The CRYRING@ESR electron cooler as internal target for atomic physics experiments

Claude Krantz[1,a], Elena-Oana Hanu[1,2,3], Mirko Looshorn[4,5], Athanasios Koutsostathis[6,11], Zoran Andelkovic[1], Carsten Brandau[1], Håkan Danared[7], Svetlana Fedotova[1], Wolfgang Geithner[1], Volker Hannen[8], Frank Herfurth[1], Regina Heß[1], Wolfgang Kaufmann[1], Ingrid Kraus[1], Michael Lestinsky[1], Esther Babette Menz[1,9], Jon Roßbach[1], Reinhold Schuch[10], Sergiy Trotsenko[1], Gleb Vorobyev[1], Michael Waider[4,5], Shu-Xing Wang[4,5], and Stefan Schippers[4,5]

[1] GSI Helmholtz Centre for Heavy-Ion Research, 64291 Darmstadt, Germany
[2] Johann Wolfgang Goethe-Universität Frankfurt, 60323 Frankfurt am Main, Germany
[3] Helmholtz-Institut Jena, 07743 Jena, Germany
[4] I. Physikalisches Institut, Justus-Liebig-Universität Gießen, 35392 Giessen, Germany
[5] Helmholtz Forschungsakademie Hessen für FAIR, GSI Helmholtz Centre for Heavy-Ion Research, 64291 Darmstadt, Germany
[6] Department of Physics, National Technical University of Athens, 15780 Zografou, Greece
[7] European Spallation Source, 221 00 Lund, Sweden
[8] Institut für Kernphysik, University of Münster, 48149 Münster, Germany
[9] Institute for Nuclear Physics, University of Cologne, 50937 Cologne, Germany
[10] Department of Physics, University of Stockholm, 106 91 Stockholm, Sweden
[11] Present Address: Karlsruhe Institute of Technology, 76344 Eggenstein-Leopoldshafen, Germany

Received 26 February 2026 / Accepted 24 April 2026 / Published online 13 May 2026

Abstract We present developments at the electron cooler of the CRYRING@ESR storage ring aimed at improving its performance as internal target in low-energy electron–ion collision experiments. We describe recent modifications of the high-voltage and vacuum systems which lead to improved electron energy control and lower background count rates during such measurements. In a benchmark experiment on dielectronic recombination of F^{6+}, we demonstrate that a spectroscopic resolution equivalent to transverse and longitudinal thermal electron energy spreads of ≈ 1 meV and ≈ 45 μeV, respectively, can be achieved under optimum conditions. This surpasses system performance observed previously in similar experiments.

1 Introduction

Electron cooling is a method of enhancing the phase-space density of protons or ions stored in circular accelerators. Initially proposed in 1966 [1], electron cooling was quickly adopted at many medium energy (∼ 1 . . . 100 MeV/u) ion storage rings [2–6], where it is especially efficient and relatively easy to implement. More recently, the method has been extended also to much higher [7, 8] and much lower [9–11] ion energies. Essentially, an electron cooler consists of a single-pass electron beam overlapping the stored-ion beam coaxially and at equal velocity in a straight section of the ring. In the co-moving frame of the beams, the electrons are characterised by a lower temperature compared to the ions. Electron–ion scattering thus leads to energy transfer towards the electron medium, damping off-axis or off-momentum ion motion, like betatron or synchrotron oscillations [12, 13].

Beyond the cooling application, their merged-beams configuration enables the use of electron coolers as experimental setups for studies of low-energy electron–ion collisions. By offsetting the electron velocity from that of the ions, the cooler becomes a free-electron target of finely adjustable collision energy [14]. In operation with atomic ions (retaining a residual electronic shell), this electron-target mode has been used very successfully to study resonant processes in electron–ion collisions, like dielectronic recombination (DR) [15, 16]. DR is an important

[a] e-mail: c.krantz@gsi.de (corresponding author)

recombination pathway in many natural and technical plasmas, but can be challenging to predict numerically, especially if near-zero-energy resonances are involved. Experimental data on low-energy DR are valuable for plasma modelling, development of atomic structure codes, and QED tests [17–20].

In this paper, we demonstrate and discuss improved electron-target operation of the CRYRING@ESR electron cooler. In Sect. 2, we lay out the key requirements for optimal performance of the cooler in operation as a target for DR experiments. We also present a number of recent technical enhancements aimed specifically at electron-target operation, including new electrodes for electron energy control and improved vacuum systems. In Sect. 3, we present an experiment on DR of lithium-like $^{19}F^{6+}$ which serves us as benchmark to quantify performance of the cooler in target mode. In Sect. 4, we analyse and discuss the experimental results, mainly with regard to the energy resolution achieved. Section 5 concludes with a summary and outlook onto possible further upgrades of the system.

2 Methods

2.1 The CRYRING@ESR electron cooler

CRYRING@ESR is an electron cooler ion storage ring located at the international FAIR facility and operated by GSI Helmholtz Centre for Heavy-Ion Research (GSI), Darmstadt [21]. Originally developed and operated at Manne Siegbahn Laboratory (MSL), Stockholm, CRYRING is aimed at storage of $\sim 1 \ldots 10$ MeV/u heavy-ion beams [22]. As a Swedish in-kind contribution to FAIR, it has been reinstalled downstream of the higher rigidity Experimental Storage Ring (ESR) of GSI, which it now complements as a dedicated low-energy machine. By using ESR as a decelerating synchrotron, highly charged heavy ions (up to bare uranium), initially produced at higher energies by the upstream UNILAC and SIS18 accelerators, can be injected into CRYRING@ESR at typically 10 MeV/u. Additionally, a local low-energy injector linac allows operation with light ions, independently of the remaining GSI facilities [23].

Electron cooling is a key beam preparation technique at CRYRING@ESR and has been employed in all production runs since its recommissioning in 2020 [24]. Together with the ring, the electron cooler was designed at MSL [6] and has seen several upgrades already during its operation in Stockholm [25]. Most importantly, the cooler pioneered reduction of the transverse electron velocity spread by strong magnetic expansion of the beam [26]. This leads to increased electron cooling rates as well as to better energy resolution in electron-target operation, as discussed below. The higher spectroscopic resolution to be expected in DR experiments, especially when compared to the ESR electron cooler, has been a key motivation for CRYRING@ESR since the beginning of the project [21].

An overview of the electron cooler section is shown in Fig. 1. A tabulated list of practically used operating parameters has been given by Danared et al. [26]. By and large, these remain valid to this date. Electrons are emitted from a 4-mm-diameter BaO dispenser cathode kept at a temperature $T_{\text{cath}} = 1100 \ldots 1200\,\text{K}$. A superconducting solenoid creates a magnetic guiding field of typically 3.0 T at the location of the cathode. The electron gun contains two anodes for beam extraction and acceleration. The first, short anode defines the electric field at the cathode surface and thereby the extracted current. The second anode consists of a 300-mm-long drift tube [26]. Acceleration of the electrons greatly reduces their velocity spread along the forward direction, to a final value limited by competing plasma relaxation. Also taking into account the effect of beam expansion, discussed below, the longitudinal electron temperature $T_\parallel$ in the frame of the accelerated beam is given by [27]

$$kT_\parallel = \frac{k^2 T_{\text{cath}}^2}{(-eU_0)} + K \frac{e^2\, n_{e,\,\text{g}}^{1/3}}{4\pi\varepsilon_0}\ , \tag{1}$$

where k, e, and ε_0 are Boltzmann's constant, the elementary charge, and the vacuum permittivity, respectively. The first term of Eq. (1) stems from reduction of the longitudinal velocity spread under the effect of the acceleration voltage U_0. At any practically used emission currents, the second term dominates, where $n_{e,\,\text{g}}$ is the electron density at the exit of the electron gun and K a dimensionless parameter of order 1. Its precise value depends on plasma relaxation processes in the accelerating beam and thus on the details of beam formation in the electron gun. The purpose of the elongated second anode is to delay electron acceleration to the final energy. This enables intermittent plasma relaxation at some intermediate energy and yields an overall lower longitudinal temperature $T_\parallel$ of the electron beam [26]. In practice, values of $kT_\parallel$ in the range $\sim 40 \ldots 120$ µeV are observed.

At the exit of the second anode, the magnetic guiding field strength decreases by up to a factor $\chi = 100$, to typical values around 0.03 T. This so-called adiabatic expansion enlarges the diameter of the electron beam by a factor $\chi^{1/2}$, reducing its density to a final value $n_e = n_{e,\,\text{g}}/\chi$ and decreasing its transverse temperature to

$$T_\perp = T_{\text{cath}}/\chi\ . \tag{2}$$

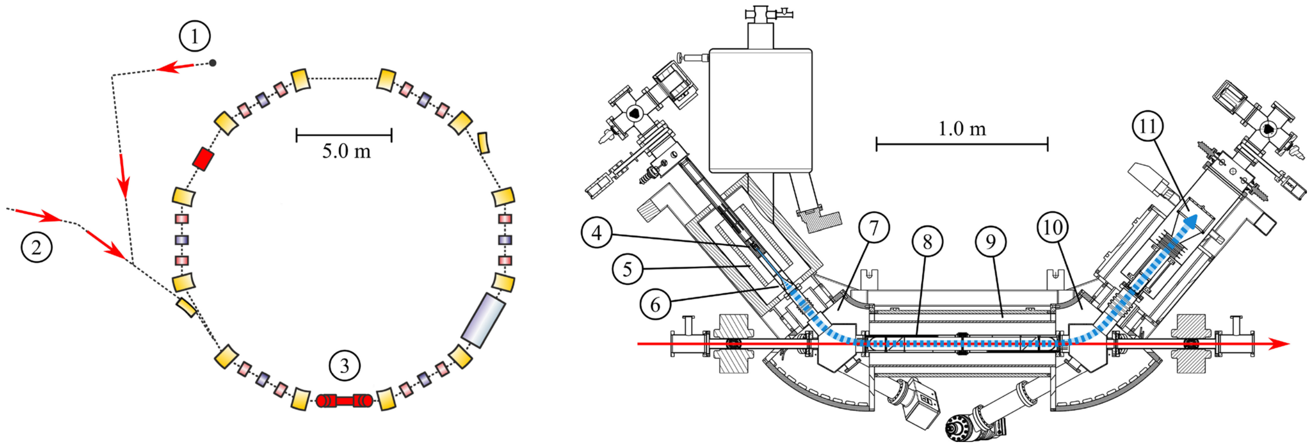

Fig. 1 Simplified overview of the magnetic lattice of CRYRING@ESR (left) and lateral cut view of the electron cooler (right). Yellow boxes represent bending dipole magnets, red and blue boxes are focussing and defocussing quadrupoles, respectively. Ion injection into the ring is possible, alternatively, from a local source (1) or from the ESR (2, not shown). In the electron cooler (3), an electron beam is extracted from a hot cathode (4) embedded in a superconducting solenoid (5). At the exit of the gun region, the electron beam is adiabatically expanded (6). A toroid magnet (7) merges the electron path (dashed blue) with that of the stored ions (solid red). After propagating along a common drift section (8) embedded in the central cooler solenoid (9), the beams are separated by another toroid (10), and the electrons are dumped at a Faraday cup (11)

For $\chi = 100$ and the cathode temperature given above, one thus expects $kT_\perp \approx 1$ meV [26].

Following the electron gun section of the cooler, a 50° toroid magnet bends the electron beam to become coaxial with the ion beam stored in the ring. After a 1.1-m-long interaction section common to both beams, the electrons are separated from the ion axis by another toroidal bend and dumped at a Faraday cup.

For electron cooler operation, the acceleration voltage U_0 of the electron gun is set such that the average velocities of electrons and ions coincide. Electron cooling then dampens betatron and synchrotron oscillations of the ions. In case of a coasting beam, it condenses the ions to a narrow forward velocity spread around the mean velocity of the electron beam.

2.2 Merged-beams electron-target operation

By offsetting the velocity of the electron beam from that of the stored ions, the cooler can also be used as a merged-beams electron target. With the ion and electron rest masses denoted by m_i and m_e, and with $\beta_i = v_i/c$ and $\beta_e = v_e/c$ being the laboratory-frame velocities of the ion and electron with respect to the speed of light c, the collision energy in the merged-beams configuration can be written as [28]

$$E_{\mathrm{cm}} = m_i c^2 (1+\mu) \left[\sqrt{1 + \frac{2\mu(\gamma_{\mathrm{rel}} - 1)}{(1+\mu)^2}} - 1 \right] , \tag{3}$$

as can be derived from four-momentum conservation. Therein, $\mu = m_e/m_i$ and $\gamma_{\mathrm{rel}} = \gamma_e\gamma_i(1-\beta_e\beta_i\cos\theta)$, with the Lorentz factors $\gamma_e = (1-\beta_e^2)^{-1/2}$ and $\gamma_i = (1-\beta_i^2)^{-1/2}$. θ is the angle between the ion and electron trajectories, ideally close to 0 for a merged-beams setup.

In the case $\theta = 0$, and by rewriting $\gamma_i = 1 + E_i/(m_i c^2)$ and $\gamma_e = 1 + E_e/(m_e c^2)$ in terms of the laboratory-frame kinetic energies E_i and E_e of ion and electron, one sees that E_{cm} vanishes for $E_e = (m_e/m_i)E_i =: E_{\mathrm{cool}}$. As it defines the condition enabling phase-space cooling of the ion beam ($\beta_e = \beta_i$), we name this particular electron energy the 'cooling energy'.

At the low storage velocities of CRYRING@ESR, viable estimates of E_{cm} can often be obtained already from the more compact classical expression, which for $\theta = 0$ reads

$$E_{\mathrm{cm}} \approx \frac{1}{2} m^* (v_e - v_i)^2 , \tag{4}$$

with the reduced mass $m^* = m_i m_e/(m_i + m_e)$. With the non-relativistic ion velocity after electron cooling given by $v_i = (2E_{\mathrm{cool}}/m_e)^{1/2}$, one can rewrite the electron velocity in terms of some small detuning of the electron acceleration voltage U_d relative to the cooling condition as $v_e = (2E_e/m_e)^{1/2} = [2(E_{\rm cool} - eU_d)/m_e]^{1/2}$. Inserting these into Eq. (4) and expanding the resulting expression for $E_{\rm cm}$ up to second order, one finds

$$E_{\rm cm} \approx \frac{m_i}{m_i + m_e} \frac{(eU_d)^2}{4E_{\rm cool}} \approx \frac{(eU_d)^2}{4E_{\rm cool}} \ . \tag{5}$$

Equation (5) shows the advantage of the merged-beams setup regarding low target energies: for $|eU_d| \ll E_{\rm cool}$, very low collision energies can be set with great precision and accuracy. For example, at $E_{\rm cool} = 5$ keV (equivalent to $E_i/A \approx 9$ MeV/u), an easily and precisely measurable value of $U_d = -2$ V results in $E_{\rm cm} \approx 0.2$ meV.

In a DR experiment, the electron cooler has to fulfil its roles as beam cooling device and internal electron-target quasi-simultaneously. At CRYRING@ESR, this is achieved by rapidly alternating the electron energy (on timescales of few ms) between the 'cooling' condition (defined by $E_{\rm cool}$) and a set of 'probing' energies yielding the desired range of target energies $E_{\rm cm}$ according to Eq. (3) [23, 24, 28]. The technique exploits the fact that there is some inertia in the response of the cooled ion beam to a sudden change in electron velocity. While the interleaved 'probing' energy phases do reduce the time-averaged electron cooling rate somewhat, low longitudinal and transverse ion emittances can be maintained overall during the DR measurement.

Ions capturing an electron in the target (e.g. through DR) initially maintain their trajectory and velocity, as the momentum transfer related to the recombination process is negligible compared to their forward momentum in the laboratory frame. However, because of their charge state, now decremented by one, their magnetic rigidity differs from that of the stored ions, and the product beam separates from the storage orbit at the bending dipole magnet following the cooler section. Thereafter, the product ions can be intercepted by a single-particle detector [23], and their production rate $R(E_{\rm cm})$ measured by a data acquisition system synchronised with the fast energy modulation of the electron beam. After suitable background subtraction and normalisation (see Sect. 3), this yields the experimental merged-beams rate coefficient (MBRC) $\alpha(E_{\rm cm})$ of the observed process [28].

2.3 Energy resolution

The energy resolution that can practically be achieved in the MBRC is limited by the spread of electron–ion collision velocities in the electron cooler. Generally, a resonance feature in collision velocity space that can be described by a cross-section $\tilde{\sigma}(v)$ is convolved with the collision velocity distribution $f(\vec{v},\, v_{\rm rel})$ to the observable MBRC

$$\alpha(v_{\rm rel}) = \int \tilde{\sigma}(v)\, v\, f(\vec{v},\, v_{\rm rel})\, {\rm d}^3 v \ , \tag{6}$$

with $\vec{v}$ being the electron–ion collision velocity, and with the definitions $v = |\vec{v}|$ and $v_{\rm rel} = c(1 - \gamma_{\rm rel}^{-2})^{1/2}$, $\gamma_{\rm rel}$ being connected to $E_{\rm cm}$ via Eq. (3). $E_{\rm cm}$ now denotes the collision energy *set-point* corresponding to a certain acceleration voltage detuning U_d of the electron beam. In an idealised merged-beams configuration, the velocity distribution is defined solely by the thermal velocity spread of the electrons, which, after electron cooling is much larger than that of the ions. In this approximation, one usually assumes the collision velocity distribution to be described by a Gaussian density function in the frame of the colliding beams [15]:

$$f(\vec{v},\, v_{\rm rel}) = \frac{m_e}{2\pi k T_\perp} \left(\frac{m_e}{2\pi k T_\parallel} \right)^{1/2} \exp\left(-\frac{m_e v_\perp^2}{2kT_\perp} - \frac{m_e (v_\parallel - v_{\rm rel})^2}{2kT_\parallel} \right) . \tag{7}$$

Therein, the collision velocity is expressed in cylindrical coordinates as $\vec{v} = (v_\perp,\, \phi,\, v_\parallel)$, with $v_\perp$ and $v_\parallel$ being the radial and axial coordinates with respect to the beam direction, and ϕ the azimuth angle. Along the transverse and longitudinal directions, the distribution is centred at $v_\perp = 0$ and $v_\parallel = v_{\rm rel}$, respectively. The velocity spreads are defined by the electron temperatures as given by Eqs. (1) and (2). Because $kT_\parallel \ll kT_\perp$ the distribution is flattened in the direction of the beams. It is implicitly made use of the facts that $m_e \ll m_i$ and that $E_{\rm cm} \ll m_e c^2$.

If, in terms of the collision energy $E = m_e v^2/2$, a resonance $\tilde{\sigma}$ is narrow compared to the energy resolution of the setup, it can be approximated by a delta function $\sigma(E) = S_{\rm res}\delta(E - E_{\rm res})$ with resonance strength $S_{\rm res}$ and energy $E_{\rm res}$. With $f(\vec{v},\, v_{\rm rel})$ from Eq. (7), ${\rm d}^3 v = v_\perp {\rm d}v_\perp {\rm d}v_\parallel {\rm d}\phi$, and by substituting, non-relativistically, $v = (2E/m_e)^{1/2}$ and $v_{\rm rel} = (2E_{\rm cm}/m_e)^{1/2}$, Eq. (6) can then be solved analytically, yielding the MBRC line profile

$$\alpha_\delta(E_{\rm cm}) = \frac{S_{\rm res}}{kT_\perp\xi}\left(\frac{E_{\rm res}}{2\,m_e}\right)^{1/2}\exp\left(-\frac{E_{\rm res}-E_{\rm cm}/\xi^2}{kT_\perp}\right) \times\left[\mathrm{erf}\left(\frac{\sqrt{E_{\rm res}}+\sqrt{E_{\rm cm}}/\xi^2}{\sqrt{kT_\parallel}/\xi}\right)+\mathrm{erf}\left(\frac{\sqrt{E_{\rm res}}-\sqrt{E_{\rm cm}}/\xi^2}{\sqrt{kT_\parallel}/\xi}\right)\right], \tag{8}$$

with $\xi = (1 - T_\parallel/T_\perp)^{1/2}$ [14, 29]. This electron-temperature-related line broadening is asymmetric around the resonance energy $E_{\rm res}$ and characterised by a full width at half maximum of [30]

$$\Delta E_{\rm cm} = \left[(kT_\perp \ln 2)^2 + 16\,E_{\rm cm}kT_\parallel \ln 2\right]^{1/2}. \tag{9}$$

Resonances with $E_{\rm res} < kT_\perp$ are practically unresolvable, as the transverse velocity spread stretches their line profiles all the way down to $E_{\rm cm} = 0$ eV. For $E_{\rm res} \gg (kT_\perp)^2/(kT_\parallel)$, the right-hand term in Eq. (9) dominates and the resolution is defined by the longitudinal velocity spread.

In reality, several other effects can broaden the true collision velocity spread beyond that of the pure thermal electron distribution as described by Eq. (7):

1. Because of the space charge of the electrons, their kinetic energies are defined by a repulsive potential $U_{\rm sc}$ in addition to the acceleration voltage U_0: $E_e = -e(U_0 - U_{\rm sc})$ [28]. The value of $U_{\rm sc}$ depends on the radial distance to the electron beam axis. Any angular misalignment between the electron and ion beams thus results in a virtual broadening of the longitudinal velocity spread [15].
2. Inhomogeneities of the magnetic guiding field in the cooler section have a similar effect on the transverse collision velocities. As any residual curvature of the magnetic field is followed by the electrons, but not by the ions, it appears like a virtual broadening of the transverse electron velocity distribution as an ion travels along the cooler [6]. Curvature of the field in the toroidal sections cannot be fully avoided and must be accounted for in data analysis [31], as will be discussed in Sect. 4.
3. Lacking control of the detuning component of the acceleration voltage (U_d in Eq. (5)) leads to instability of the target energy $E_{\rm cm}$, blurring the experimental energy resolution [28]. Technical sources of such instability can be high-voltage (HV) supply ripple, or suboptimal step-response of the HV systems to the rapid sequence of ‘cooling’ and ‘probing’ set-points [32]. Due to the finite length of the drift tubes used to apply the detuning voltage U_d, the latter may vary along the beam-overlap region. Also this effect must be carefully taken into account during data analysis [31]. Another source of $E_{\rm cm}$ instability can be trapping of ionised residual gas in the electron beam, leading to partial cancellation of the electron space charge [15].
4. Finally, operation of the cooler as a target means to temporarily give up beam cooling. As soon as the electron velocity is detuned from that of the ion beam, the latter starts to accelerate under the effect of the electron drag force, and its velocity distribution starts to broaden by intra-beam scattering. Both effects can limit the achievable DR resolution, and minimising them requires careful optimisation of the time structure of the alternating ‘cooling’ and ‘probing’ set-points applied to the electron beam energy [31].

Most of these additional contributions to the longitudinal and transverse collision velocity spreads are non-thermal in nature. However, their effects on MBRC line-broadening are often indiscernible from an overall wider thermal velocity distribution, so that they mimic larger values of $kT_\parallel$ and $kT_\perp$ in Eqs. (8) and (9).

2.4 Fast electron energy control

The rapid alternation of the electron beam energy between the ‘cooling’ and ‘probing’ set-points is realised by adding the output of a fast HV amplifier U_d to the base acceleration voltage provided by the electron cooler's main HV supply (U_0). Usually, the highly stabilised voltage U_0 is set so that with $U_d = 0$ V, the electron energy on axis of the beam corresponds to the cooling energy: $E_{\rm cool} = -e(U_0 - U_{\rm sc}(0))$.

After electron cooling is complete, a rapid ($\sim$ 1 ms) detuning to some value $U_d \neq 0$ V temporarily leads to a changed electron energy $E_e = -e(U_0 + U_d - U_{\rm sc}(U_d))$. Because the response of the ion velocity to the electron cooler set-point is slow, one can compute the collision energy $E_{\rm cm}$ from Eq. (3)[1] with $\gamma_i = 1 + E_{\rm cool}/(m_e c^2)$. After typically $\sim$ 10 ms, another fast jump of the HV amplifier back to $U_d = 0$ V is performed, so that beam cooling is maintained.

[1]Note that the approximative formula (5), while useful for quick estimates, among other things also neglects the fact that $U_{\rm sc}(0) \neq U_{\rm sc}(U_d)$ and is thus not suited for precision data analysis.

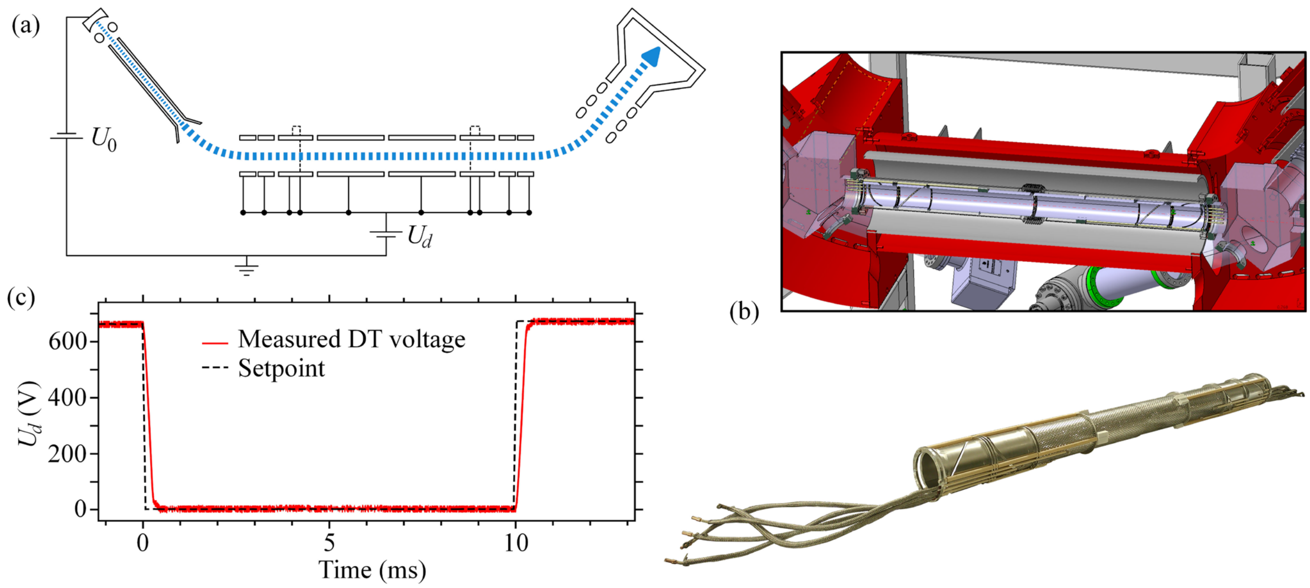

Fig. 2 The recently installed drift-tube/BPM setup of the CRYRING@ESR electron cooler. **a** Simplified wiring diagram (not to scale) illustrating definition of the overall acceleration potential by combination of the base HV supply (U_0) and the fast HV amplifier (U_d). The drift and pickup electrodes all have individual vacuum feedthroughs (dots) so that, alternatively, only a subset can be biased to U_d. **b** 3D CAD model and photograph of the drift-tube/BPM insert. **c** Response of the drift-tube voltage to rapid falling and rising changes of the set-point (all electrodes connected)

In previous implementation of the technique at CRYRING@ESR, the base HV supply and the fast HV amplifier were connected in series, so that, together, they biased the electron-emitting cathode to a total negative potential difference of $U_0 + U_d$ with respect to ground [23, 24, 28]. This mode of operation limits the slew rate of the fast voltage modulation U_d, as the full capacity of the cooler HV terminal must be charged and discharged. Also, instability of the sum acceleration voltage has often been observed, which was attributed to interference between the fast HV amplifier and the voltage regulation circuit of the base HV supply [32].

Recently, the electron cooler has therefore been upgraded with a set of HV-capable drift-tube electrodes in the merged-beams section, as depicted in Fig. 2a and b. The newly added drift tubes complement preexisting sets of horizontal and vertical beam position monitors (BPMs) at both ends of the cooler solenoid which have been modified to now support bias voltages up to several kV [32]. The resulting drift-electrode structure covers the entire length (1.1 m) of the central cooler solenoid. By connecting the output of the fast detuning voltage U_d to all or a subset of the drift electrodes, the 'probing' electron energy $E_e = -e(U_0 - U_d - U_{\rm sc}(U_d))$ can be created locally in the interaction section, while keeping the voltage applied to the cathode statically at U_0. Note that, to obtain values $E_e > E_{\rm cool}$, the polarity of U_d now needs to be reversed with respect to that of U_0 (see Fig. 2a).

Separation of electron acceleration into two independent systems avoids technical interference between the two HV supplies, so that the highly stabilised U_0 supply can be used to its full level of precision (relative ripple $\lesssim 10^{-5}$). To take advantage of the lower capacity of the new energy-modulation system, the formerly used KEPCO BOP-1000M HV amplifier has been replaced by a higher bandwidth HiVolt HA2B5-S ($\pm$2000 V). The step-response of the new system is displayed in Fig. 2c. In both directions, the measured slew rate is 2.4 kV/ms with all drift electrodes connected, and the drift-tube voltage U_d settles at a new value in < 1 ms, even for large steps.

2.5 Electron cooler vacuum systems

Good vacuum in the electron cooler section is mandatory for effective use as electron target for DR experiments. Capture of electrons from residual-gas atoms or molecules by the low-energy ions not only limits their storage lifetime in the ring [23], but also is not easily distinguishable from recombination with free electrons in the cooler beam. The product rates from residual-gas charge exchange thus appear as detector background that must be subtracted to obtain the true MBRC. If background rates are exceedingly high, their statistical fluctuations mask detector counts from weak DR resonances, thus imposing a lower limit on the cross-sections that can practically be measured in the experiment.

Additionally, residual-gas particles can accumulate in the negative space charge potential of the cooler beam if ionised by electron impact. Besides the background problem in DR measurements, these trapped ions can partly neutralise the electron space charge, leading to unstable values of U_{sc} and the aforementioned adverse effect on the longitudinal velocity spread.

Generally, creating good vacuum conditions ($\sim 10^{-11}$ mbar) in an electron cooler is challenging as, both, the heat from the hot cathode and the power of the electron beam itself cause desorption from exposed surfaces. Also, critical parts of the vacuum vessel are almost fully surrounded by the electron-guiding solenoid and toroid magnets (see Fig. 1), which prevents maintenance access. In case of the CRYRING@ESR cooler, the vacuum conditions had been severely compromised after the bake-out heater of the merged-beams vacuum pipe had failed in 2020, shortly after commissioning. While the resulting bad vacuum pressure did not prevent successful operation altogether, the associated detector background in electron-target experiments has been noted as a limiting factor, especially regarding DR measurements [20, 23, 28].

Normally inaccessible because of the surrounding magnet structure, the defective heater could only be replaced in 2023, when a long maintenance break of GSI/FAIR provided the opportunity to fully disassemble the electron cooler. In the process, most of the vacuum pumps were replaced by more modern systems, and new extremely high vacuum gauges were installed up- and downstream from the interaction section. To compensate for the greater surface area of the new drift-tube/BPM insert—installed at the same time—the central beam pipe (but not the electrode structure itself) was coated with non-evaporable getter (NEG) material.

In an effort to suppress residual-gas ion trapping in the electron beam, a pair of clearing electrodes have been installed at the entrance to the Faraday cup section of the cooler. They create an electric field transverse to the electron beam, allowing trapped ions to escape from the space charge well. Alternatively, a pair of the upgraded BPM electrodes in the merged-beams section can be used for the same purpose.

By establishing new bake-out procedures, with higher activation temperatures applied to the internal NEG pumps, the vacuum pressure in the electron cooler was improved by a factor $\gtrsim 6$, and was again on-par with the neighbouring sections of CRYRING@ESR during the 2025 GSI/FAIR experimental run. During the experiment described below, an H_2 equivalent pressure of $\sim 1 \times 10^{-11}$ mbar was measured during electron beam operation at $E_{\mathrm{cool}} \approx 5$ keV and 20 mA of emission current.

3 Experiment

To determine optimal settings of the electron cooler for use as internal target in electron–ion collision experiments, and to verify the good working condition of the technical upgrades introduced above, we conducted an experiment on DR of lithium-like $^{19}F^{6+}$. Theoretically well understood, the MBRC of that process has become a popular benchmark for quantifying the experimental resolution of a DR setup, and has been measured at several electron coolers, including the one at CRYRING before its transfer from MSL to GSI/FAIR [33–36].

DR of F^{6+} proceeds via a set of doubly excited, auto-ionising levels $\left(F^{5+}\right)^{**}$ of the product ion F^{5+}:

$$F^{6+} + e \rightleftharpoons \left(F^{5+}\right)^{**} \rightarrow F^{5+} + \sum_j \gamma_j \; . \tag{10}$$

Only the F^{5+} daughter beam is detected in our setup [23], while the spectrum of de-excitation photons $\sum_j \gamma_j$ is not observed. At collision energies $E_{\mathrm{cm}} < 0.6$ eV, DR leads to a prominent array of resonances, all occurring from capture of the electron into the $n = 6$ shell of F^{5+} [34]. Especially the $(2p_{3/2}\,6p_{1/2})_2$ level of F^{5+} is associated with a strong, well-isolated DR resonance at $E_{\mathrm{cm}} \approx 10$ meV. Its predicted natural line-width of 100 µeV is of the same order as $kT_{\parallel}$ at even the lowest temperature electron coolers. Its profile, as appearing in the MBRC, is thus strongly defined by the longitudinal and transverse collision velocity spreads, much similar to Eq. (8).

In our experiment, we extracted a beam of $^{19}F^{6+}$ from the electron cyclotron resonance ion source of CRYRING@ESR. The ions were pre-accelerated to a kinetic energy of 300 keV/u in the radio-frequency quadrupole linac of the local injector branch. After multi-turn injection into the ring, the ions were synchrotron-accelerated to energies of either 9 MeV/u or 4 MeV/u.

During the experiment, the F^{6+} ions were then stored at constant energy under coasting-beam conditions, i.e. with phase-focussing via the radio-frequency (rf) acceleration gaps of the ring switched off. The ions were electron-cooled for 2 s, after which the energy of the electron beam was quickly cycled through the set of 'probing' and 'cooling' energies, as described above. The F^{5+} product ions were counted by a YAP:Ce scintillator detector [23] with practically 100 % efficiency. For background subtraction, the 'probing' energies also contained a repeating subset of 'reference' E_{cm} values, where no significant contribution of DR to the measured MBRC was expected. After ≈ 30 s, a new injection cycle was started to compensate for the loss of stored ions through electron recombination and residual-gas collisions.

The data acquisition and analysis have been described in detail by Brandau et al. [28]. With the background-subtracted DR product rate denoted by $R(E_{\mathrm{cm}})$, the experimental MBRC $\alpha(E_{\mathrm{cm}})$ is obtained by normalisation to

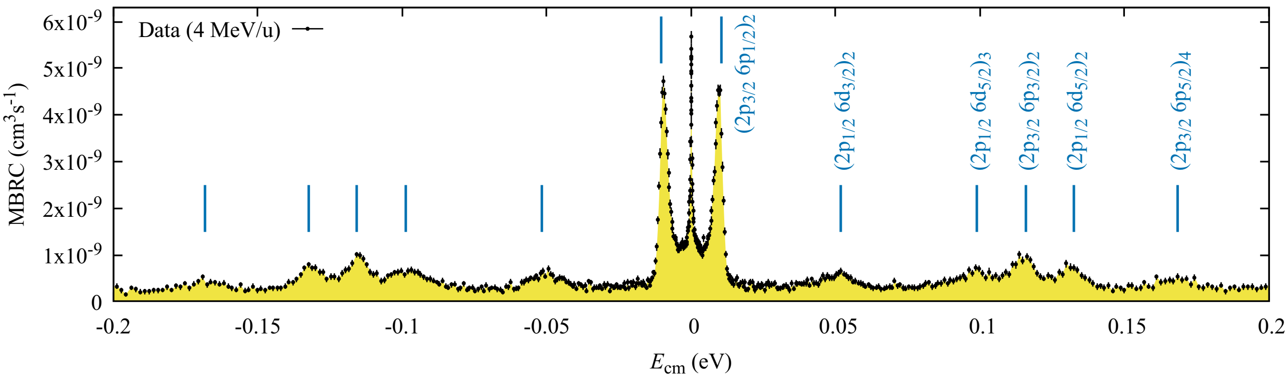

Fig. 3 Example of a measured recombination rate coefficient for $F^{6+} + e \rightarrow F^{5+}$ at lowest energies. Negative or positive values of $E_{\rm cm}$ represent electron–ion collisions with $\beta_e < \beta_i$ or $\beta_e > \beta_i$, respectively. The labels indicate expected DR resonance energies as per Tokman et al., 2002 [34], and Lestinsky, 2007 [35]

the electron density n_e and the number of stored ions N_i [29]:

$$\alpha(E_{\rm cm}) = \frac{R(E_{\rm cm})}{n_e(E_{\rm cm})\, N_i} \times \frac{C}{L} \times \frac{1}{1-\beta_i\beta_e(E_{\rm cm})} \,. \tag{11}$$

The additional factor C/L is the ratio between the length of the stored-ion orbit in the ring ($C = 54.2$ m) and the length L along the cooler section where, within the experimental resolution, electron–ion collision energies correspond to the set $E_{\rm cm}$ value. In previous experiments, $L = 0.9$ m has been found to be a good approximation [28] and we also adopt it for initial analysis of our F^{6+} experiment. This assumption will be discussed in detail in Sect. 4. The last factor in Eq. (11) is a relativistic correction, always close to 1 for CRYRING@ESR.

The electron density $n_e(E_{\rm cm})$ can be calculated from the cooler electron current measured at the Faraday cup, the known diameter of the electron beam, and β_e [28]. For a given $E_{\rm cm}$ set-point, it is assumed to be constant over the target length L. Values of $n_e \approx 2.4 \times 10^6$ cm^{-3} and $n_e \approx 3.2 \times 10^6$ cm^{-3} were used for the 9-MeV/u and 4-MeV/u ion energies, respectively.

For highly charged heavy ions, N_i is usually obtained from the directly measured current of the stored beam in the ring [28]. For our low-charged and relatively low-intensity F^{6+} beam, the associated dc-transformer proved not sufficiently precise. CRYRING@ESR features more sensitive beam diagnostics for rf-bunched beams, which are however unsuitable for DR experiments as their momentum spread is enlarged by synchrotron oscillation. In dedicated accelerator cycles with rf-bunching enabled, we thus calibrated the average count-rate of an ionisation beam-profile monitor (IPM) against an integrating bunch-current transformer. Subsequently, we could use the IPM count-rate as proxy for N_i also for the coasting beams used in the experiment. Typically, $5 \ldots 7 \times 10^6$ ions were stored directly after acceleration.

A 900-mm-long subset of the drift-tube structure was used for applying the fast modulation of $E_{\rm cm}$. The true drift-tube voltage U_d applied at given set-point of the fast HV amplifier was calibrated off-line against a precision voltage divider of $< 10^{-5}$ relative accuracy (named FC-20 [24, 28]), connected to the drift-tube subset. In the experiment, data taking started only 0.9 ms after stepping to a new $E_{\rm cm}$ set-value in order to account for the time needed for the voltage U_d to actually settle (see Sect. 2.4). Real-time readout of the FC-20 divider in-sync with the fast energy modulation is under development, but was not yet available during the F^{6+} experiment.

Any one value of $E_{\rm cm}$ can physically be obtained in two different ways: by setting the electron velocity either higher or lower than that of the ions. Conventionally, we map conditions with $\beta_e < \beta_i$ to negative values of $E_{\rm cm}$. During the experiment, we repeatedly scanned the region $-0.2\,\text{eV} \lesssim E_{\rm cm} \lesssim 0.7\,\text{eV}$. Including a range of negative $E_{\rm cm}$ values in the scan is beneficial, as the symmetry of the low-energy DR spectrum around $E_{\rm cm} = 0$ eV, as illustrated in Fig. 3, then allows very precise determination of $E_{\rm cool}$ (and thus β_i) during data analysis [20]. The central peak at $E_{\rm cm} = 0$ eV is due to (non-resonant) radiative recombination of F^{6+} in the cooler electron beam. After typically 2 to 3 h of data accumulation, the statistical quality of the measured DR spectra was sufficient to unambiguously determine the width of the prominent $(2p_{3/2}\,6p_{1/2})_2$ line.

The measurements were repeated every few hours, while varying the experimental parameters and monitoring the line-width of the $(2p_{3/2}\,6p_{1/2})_2$ resonance. Using the latter as benchmark for the resolving power of the setup, the resolution-limiting effects listed in Sect. 2.3 could be studied and iteratively minimised.

The greatest improvements were obtained by optimising the axial alignment between electron and ion beams as well as the time structure of the sequence of 'cooling' and 'probing' acceleration voltages. The former was achieved

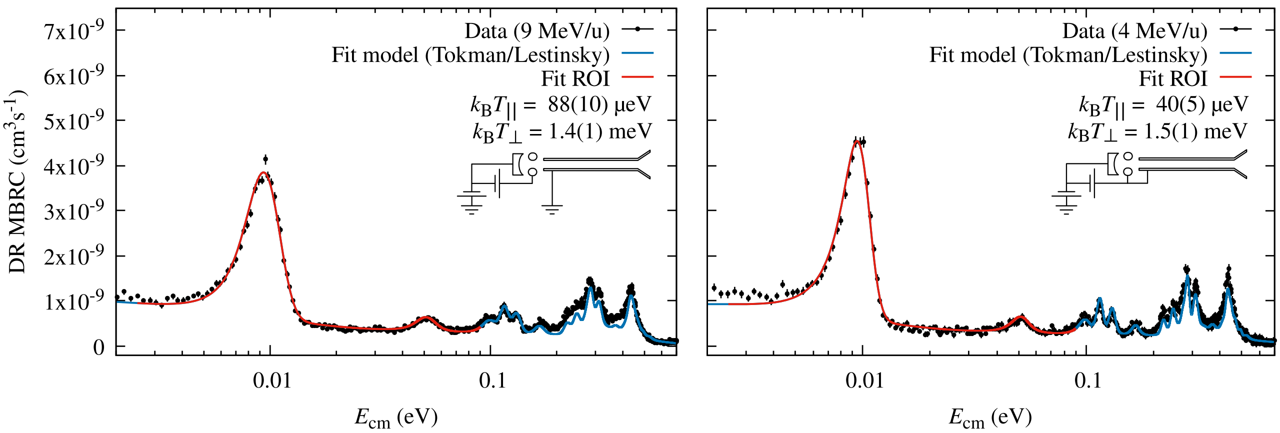

Fig. 4 Experimental DR MBRC for $F^{6+} + e \rightarrow F^{5+}$, measured at ion energies of 9 MeV/u (left) and 4 MeV/u (right), respectively. The low ion energy case allows for a different configuration of the electron gun, as depicted in the insets and discussed in the text. The solid blue curves are fitted model DR spectra convolved with the given longitudinal and transverse thermal electron energy spreads. The red parts of the curves indicate the fit regions-of-interest

through steerer coils allowing adjustment of the transverse positions and angles of the electron beam in the merged-beams section. For the latter, it was found that increasing the dwell time at a 'cooling' step from initially 10 ms to 15 ms, thus increasing the time-averaged electron cooling force, improved the resolution at low E_{cm}. With the 'probing' voltage additionally alternating between the fixed reference value and the actual DR measurement scan, this resulted in a repeating cooling–reference–measurement pattern of $(15 + 10 + 10)$ ms duration.

Some experimental parameters were also found to have little to no effect on the resolution. The newly installed clearing electrodes (see Sect. 2.5) were powered, but no effect on the spectral resolution or on the stability of the cooled beam could be observed. Correction coils in the central solenoid, specifically installed for improving the homogeneity of the magnetic field [6], apparently could only worsen the experimental resolution. The final settings for their currents, found through systematic variation, were so close to 0 A that their effect on the field geometry is believed to have been negligible in the measurements discussed below.

The electron gun always operated at magnetic expansion $\chi = 100$, so the true transverse electron temperature $T_\perp$ from Eq. (2) is expected to have been the same throughout the experiment. The reason for the two different ion energies, 9 MeV/u and 4 MeV/u, is that the corresponding E_{cool} values of ≈ 5.0 keV and ≈ 2.2 keV, respectively, allowed us to test two different modes of beam acceleration in the electron gun. Because of technical limitations, the second, tube-shaped anode of the gun, as described in Sect. 2.1, cannot be biased by more than ≈ 2.5 kV with respect to the surrounding vacuum chamber. When high values of U_0 are applied to the cooler HV terminal, this anode is thus usually grounded. As a consequence, the electrons are then accelerated to E_{cool} in a single ~ 1 cm short gap, resulting in a large coefficient K in Eq. (1) and a correspondingly high value of $kT_\parallel$. For low-voltage operation of the cooler, the two gun anodes can instead be connected in parallel, and biased just high enough with respect to the cathode potential to extract the desired electron current (≈ 500 V for the 18 mA used in this experiment). The resulting two-step acceleration of the electron beam is expected to lead to lower values of $kT_\parallel$, as described in Sect. 2.1 [26].

4 Results and discussion

Figure 4 shows the measured low-energy DR MBRC for the two different ion energies and electron gun configurations, after optimisation of all other parameters of the experimental setup, as described above. To quantify the spectral resolution achieved, we fitted the data with a theoretical spectrum of all $n = 6$ DR resonances of F^{6+}, numerically convolved with the longitudinal and transverse electron temperatures. Resonance energies as well as line intensities and natural widths are mostly taken from Tokman et al., 2002 [34]. For the low-energy levels $(2p_{3/2}\,6p_{1/2})_2$ to $(2p_{1/2}\,6d_{5/2})_2$, we refined the theory spectrum by empirical data, adopting line positions and strengths measured by Lestinsky using the high-resolution Electron Target at the Heidelberg TSR storage ring [35]. Besides $kT_\parallel$ and $kT_\perp$, a global amplitude scaling and a tilted background level are free parameters in the fit. The latter allow the model to adapt to potential systematic errors in background subtraction and normalisation of the data.

The fit results are shown in Fig. 4. The temperature-convolved model spectrum is represented by the solid blue/red curves. Only the $(2p_{3/2}\,6p_{1/2})_2$ resonance at ≈ 10 meV displays a clear asymmetry due to $kT_\perp > kT_\parallel$. To obtain a meaningful value for $kT_\perp$, only the lowest energy part of the spectrum ($E_{\rm cm} \leq 0.09$ eV), as highlighted in red, was considered as region-of-interest (ROI) in the fit routine. The best-fit values of $kT_\parallel$ and $kT_\perp$ are quite strongly correlated with those for the (potentially tilted) background level. The uncertainties given in Fig. 4 reflect that correlation in addition to the asymptotic error bars.

In both cases of Fig. 4, the fit curves needed to be scaled-down by a factor ≈ 0.67 in amplitude to match our data, indicating a 33% deviation in normalisation compared to the Heidelberg experiment [35]. This can mostly be explained by the fact that our usual target length $L = 0.9$ m, adopted in Eq. (11) for this initial analysis, is no longer valid at the very low $E_{\rm cm}$ here discussed.

As mentioned in Sect. 2.3, the ideal merged-beams configuration, with perfectly coaxial electron and ion beams, can be strictly achieved only at centre of the cooler section. Especially since the correction coils of the main cooler solenoid could not be used effectively (see Sect. 3), the curvature of the magnetic guiding field from the toroidal sections of the cooler reached well into the straight solenoid region [6]. The resulting vertical bend of the electron beam and the average electron–ion collision angle θ are shown in Fig. 5 as functions of the longitudinal coordinate along the cooler. A parametric expression for the beam geometry has been given by Brandau et al. [28]. With a diameter of the electron-emitting cathode of 4 mm (cf. Fig. 6) and $\chi = 100$, the expanded electron beam is 40 mm wide, and quite large values of θ occur before overlap between electrons and the ion beam (assumed at $y = 0$ mm) is lost. In addition, β_e changes along the overlap region. Besides the obvious effect of the detuning voltage U_d, applied only to the central 900 mm of the drift-tube structure, the radial dependence of the electron space charge $U_{\rm sc}(y)$ must be accounted for as the dislocation y between the two beams increases towards the edge of the overlap region.

The collective effect of the electron beam and drift-tube geometries on the actual value of $E_{\rm cm}$ as a function of the longitudinal coordinate is displayed in the lowermost panel of Fig. 5. The red curves, corresponding to four different set-values of $E_{\rm cm}$ at the cooler centre, illustrate how the target length L effectively depends on

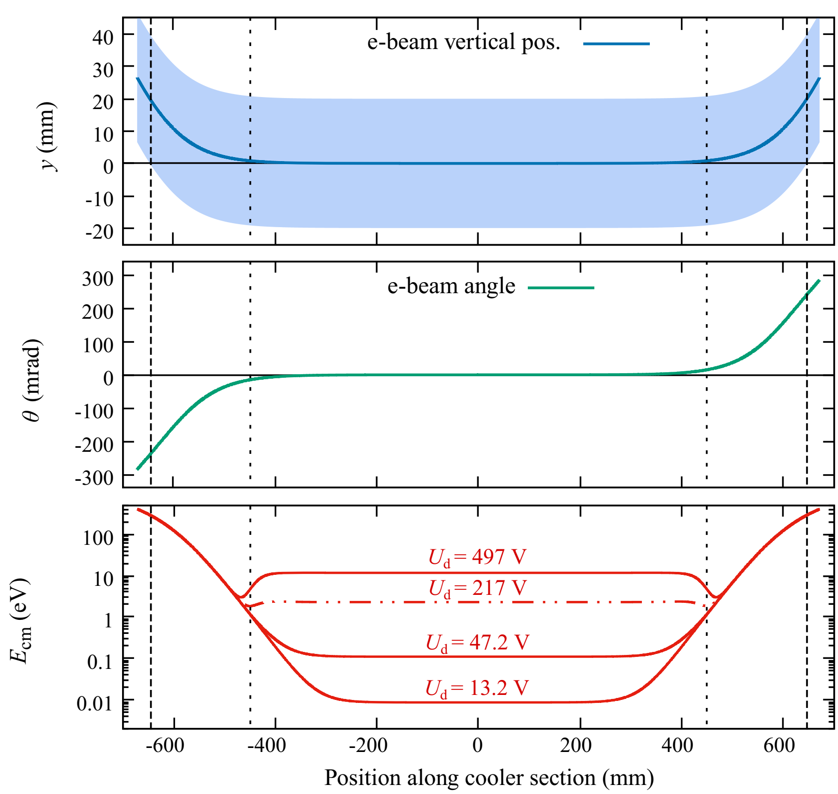

Fig. 5 Effect of the merged-beams geometry on the collision energy $E_{\rm cm}$ along the cooler section. Top: vertical dislocation of the electron beam with respect to the ion axis (at $y = 0$ mm). The shaded blue region indicates the electron beam diameter. Middle: angle θ between the electron and ion beams. Bottom: resulting dependence of $E_{\rm cm}$ on the longitudinal coordinate along the ion beam for different detuning voltages U_d at $E_{\rm cool} \approx 5.0$ keV, corresponding to $E_{\rm cm}$ values of 9 meV, 110 meV, 2.3 eV, and 11.7 eV at the cooler centre. The dashed vertical lines delimit the interval where electron–ion interaction is possible. The dotted vertical lines indicate the total length of the drift tubes used for energy modulation

Fig. 6 The BaO dispenser cathode of the CRYRING@ESR cooler as seen through the viewer of a pyrometer measuring the temperature of the electron-emitting surface. The diameter of the cathode is 4 mm

those energies of interest: At higher collision energies $E_{\rm cm} \gtrsim 1$ eV, the length of the active drift-tube structure of 0.9 m might indeed have been a viable approximation for L. For low energies, however, the bend of the electron beam creates relatively large deviations of $E_{\rm cm}$ well into the drift-tube region. Especially near the 10 meV of the $(2p_{3/2}\,6p_{1/2})_2$ resonance, $E_{\rm cm}$ deviations greater than the line-width occur already at a distance of ≈ 300 mm from the cooler centre, i.e. a value $L \approx 0.6$ m would seem more appropriate here.

One way of dealing with the situation is to use the known dependence of $E_{\rm cm}$ on the longitudinal position, as illustrated in Fig. 5, to numerically deconvolve the geometry effects out of the data. The procedure relies on iterative correction of $\alpha(E_{\rm cm})$ based on the true distribution of collision energies at given set-value of $E_{\rm cm}$ and has been described, e.g. by Hoffknecht et al. [31]. It is particularly well suited for the new energy-modulation system, where the voltage U_d is applied to the drift-tube structure of the cooler. In this case, the very high collision energies occurring in the toroidal sections of the cooler are independent of the $E_{\rm cm}$ set-point (see Fig. 5). Thus, these regions contribute only a constant background to the experimental DR spectrum, which is easily handled in data analysis even though the measured $\alpha(E_{\rm cm})$—as used in the deconvolution procedure—does not extend to these very high energies.

Figure 7 again shows the low-energy DR resonance spectra measured at high and low ion energy, now deconvolved with regard to the effects of beam and drift-tube geometries. The deconvolution introduces numerical noise resulting in somewhat greater scatter of the data. The error bars, originally representing only the counting statistics, have been scaled accordingly. The same model DR spectrum as in Fig. 4 is fitted to the data. The fit ROI could be extended up to 0.2 eV as the model can now match the profiles and amplitudes of all lines simultaneously. The global amplitude scaling required to fit the data is reduced to ≈ 0.95. The remaining 5% deviation in normalisation is within the accuracy of our measurement of N_i.

As the deconvolution essentially corrects for the residual curvature of the magnetic field, the best-fit values for $kT_\parallel$ are unaffected, while those for $kT_\perp$ are significantly improved. A pyrometer-based measurement of the temperature of the electron-emitting surface of the cathode yielded a value $T_{\rm cath} = 1140 \pm 60$ K (cf. Fig. 6). With the electron gun operating at $\chi = 100$, one thus expects $kT_\perp \approx 1.0$ meV from Eq. (2), in excellent agreement with the values obtained from the fits in Fig. 7.

Keeping in mind that the theoretically predicted natural line-width of the $(2p_{3/2}\,6p_{1/2})_2$ resonance amounts to 100 µeV, we can compare the fit results for $kT_\parallel$ from Figs. 4 and 7 to the values expected according to Eq. (1). In case of the 9-MeV/u measurement, we have $n_{e,\,g} \approx 2.4 \times 10^8\,{\rm cm}^{-3}$ before beam expansion. Assuming $K \approx 1$, as suggested by molecular dynamics calculations [26], Eq. (1) yields $kT_\parallel \approx 90$ µeV, in good agreement with the experiment. Under the same assumptions, Eq. (1) would evaluate to $kT_\parallel \approx 100$ µeV for the 4-MeV/u measurement, owing to the greater electron density of $n_{e,\,g} \approx 3.2 \times 10^8\,{\rm cm}^{-3}$. That the measured value of $kT_\parallel$ is an approximate factor of 2 lower in this case suggests that two-step acceleration of the electrons leads to a reduced value of $K \approx 0.5$, in fair agreement with numerical simulations [26].

It is worth noting that, even without geometry deconvolution, the transverse, and to lesser extent also longitudinal, electron temperatures found in this work are significantly lower than those reported in equivalent experiments on F^{6+} DR conducted with CRYRING in operation at MSL. In those studies, values of $kT_\parallel = 100 \ldots 120$ µeV and $kT_\perp = 3.0 \pm 0.5$ meV had been obtained, using essentially the same methodology as we employed here [33, 34]. Especially regarding the unexpectedly large value of $kT_\perp$, possible misalignments of the cooler beam have been discussed [26]. In MSL experiments on low-energy DR of Pb^{53+}, indications of lower values $kT_\perp = 1 ... 2$ meV and $kT_\parallel \approx 80$ µeV had been found around the same time [37], in much better agreement with our results. With regard to $kT_\parallel$, a difference between the previous and present DR setups lies in the fact that, in the Stockholm experiments, no attempt was made to maintain electron cooling during the $E_{\rm cm}$ scan. While resulting changes of the average β_i during the measurement were monitored and corrected for in data analysis [33], the increase in

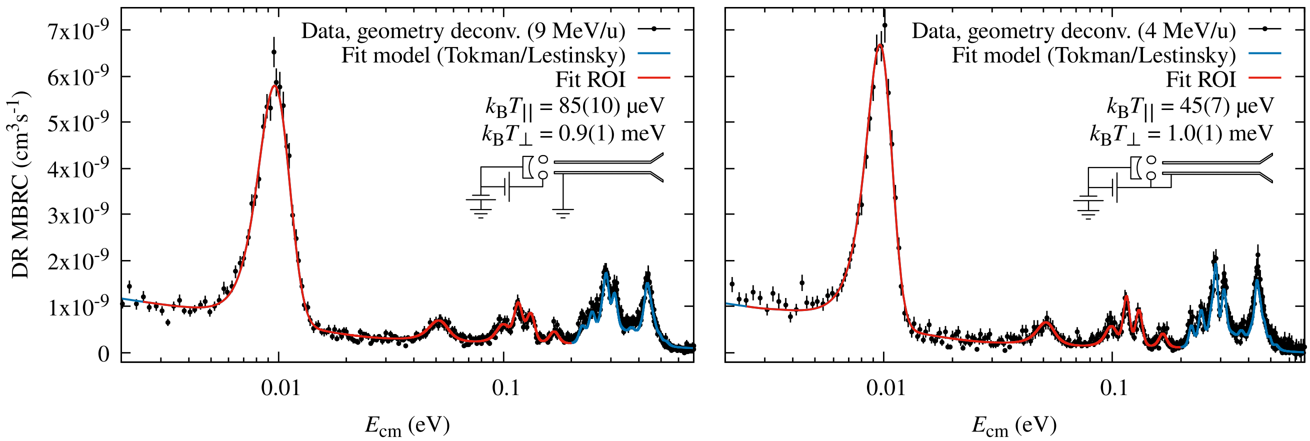

Fig. 7 Experimental DR MBRC for $F^{6+} + e \rightarrow F^{5+}$ as in Fig. 4, but numerically deconvolved such as to remove the effects of the merged-beams and drift-tube geometry. Other curves and labels are equivalent to those of Fig. 4

transverse and longitudinal ion emittance in the absence of cooling may have resulted in a broader distribution of collision energies.

5 Conclusion

We have presented the CRYRING@ESR electron cooler as a platform for experiments on low-energy electron–ion collisions. The setup is especially well suited for precision studies of electron recombination of atomic ions. We have described recently introduced technical upgrades of the cooler aimed specifically at improving its performance in this electron-target mode of operation.

As benchmark for the resolution that can be achieved in such collision experiments, we have re-measured the well-known low-energy DR resonance spectrum of F^{6+}. The measurements show excellent agreement with previous theoretical and empirical work. The energy resolution at lowest energy is equivalent to a transverse electron temperature $kT_\perp \approx 1.5$ meV, assuming perfectly coaxial beams. This exceeds previously reported performance in similar experiments. The fact that, after deconvolution of the data for effects of a realistic target beam geometry, an even lower value of $kT_\perp \approx 1.0$ meV is observed, suggests that the true transverse electron temperature is in fact in agreement with the directly measured temperature of the electron source, considering the magnetic expansion factor of $\chi = 100$. It also suggests that even better resolution at low energy could be obtained if the residual curvature of the magnetic field in the interaction region could be reduced. In that context, further studies are required to clarify why the field correction coils, installed specifically for this purpose, could not be used effectively in this experiment.

At higher collision energies, the resolution is defined by the longitudinal electron temperature. A value of $kT_\| \approx 45$ μeV is observed under optimum conditions, in reasonable agreement with theoretical predictions. At present, the improvement of $kT_\|$ by two-step acceleration of the electron beam can technically be realised only at relatively low ion energies. By wiring the second gun anode to a dedicated HV supply, this feature could—at least to some degree—be made available also at higher values of E_{cool}. Ideally, a future, revised design of the gun electrodes could allow adiabatic electron acceleration at all energies.

Acknowledgements Results are based on R&D in the context of FAIR Phase-0 at GSI. M.Lo., M.W., S.-X.W, and S.S. are grateful for funding provided by the German Ministry for Research, Technology and Space (BMFTR) within the collaborative research centre ErUM FSP T05—“Aufbau von APPA bei FAIR” (grant number 05P24RG2). The work of A.K. received funding from the European Union’s Horizon Europe Research and Innovation programme under grant agreement number 101057511. E.B.M. acknowledges support by the project “NRW-FAIR”, part of the programme “Netzwerke 2021”, an initiative of the Ministry of Culture and Science of the State of North Rhine-Westphalia. This publication is funded by the Open Access Publishing Fund of GSI Helmholtzzentrum für Schwerionenforschung.

Funding Open Access funding enabled and organized by Projekt DEAL.

Data Availability Data will be made available by the corresponding author on reasonable request.

References

1. G.I. Budker, An effective method of damping particle oscillations in proton and antiproton storage rings. At. Energy **22**(5), 438 (1967). https://doi.org/10.1007/BF01175204
2. M. Bell, J. Chaney, H. Herr, F. Krienen, P. Møller-Petersen, G. Petrucci, Electron cooling in ICE at CERN. Nucl. Instrum. Methods Phys. Res. **190**(2), 237 (1981). https://doi.org/10.1016/0029-554X(81)90288-3
3. T. Tanabe, M. Sekiguchi, K. Sato, M. Kodaira, A. Noda, J. Tanaka, H. Tsujikawa, T. Honma, M. Takanaka, Y. Hirao, Electron cooling device for TARN II. IEEE Trans. Nucl. Sci. **32**(5), 2412 (1985). https://doi.org/10.1109/TNS.1985.4333930
4. B. Franzke, The heavy ion storage and cooler ring project ESR at GSI. Nucl. Instrum. Methods Phys. Res., Sect. B **24**, 18 (1987). https://doi.org/10.1016/0168-583X(87)90583-0
5. M. Steck, G. Bisoffi, M. Blum, A. Friedrich, C. Geyer, M. Grieser, B. Holzer, E. Jaeschke, M. Jung, D. Krämer, K. Matl, W. Ott, R. Repnow, Electron cooling of heavy ions. Nucl. Instrum. Methods Phys. Res. Sect. A **287**, 324 (1990). https://doi.org/10.1016/0168-9002(90)91817-U
6. H. Danared, Electron cooling at CRYRING. Phys. Scr. **48**(4), 405 (1993). https://doi.org/10.1088/0031-8949/48/4/004
7. S. Nagaitsev, L. Prost, A. Shemyakin, Fermilab 4.3 MeV electron cooler. J. Inst. **10**(01), T01001-T01001 (2015). https://doi.org/10.1088/1748-0221/10/01/T01001
8. A.V. Fedotov, Z. Altinbas, S. Belomestnykh, I. Ben-Zvi, M. Blaskiewicz, M. Brennan, D. Bruno, C. Brutus, M. Costanzo, A. Drees, W. Fischer, J. Fite, M. Gaowei, D. Gassner, X. Gu, J. Halinski, K. Hamdi, L. Hammons, M. Harvey, T. Hayes, R. Hulsart, P. Inacker, J. Jamilkowski, Y. Jing, J. Kewisch, P. Kankiya, Kayran, D., Lehn, R., Liaw, C.J., Litvinenko, V., Liu, C., Ma, J., Mahler, G., Mapes, M., Marusic, A., Mernick, K., Mi, C., Michnoff, R., Miller, T., Minty, M., Narayan, G., Nayak, S., Nguyen, L., Paniccia, M., Pinayev, I., Polizzo, S., Ptitsyn, V., Rao, T., Robert-Demolaize, G., Roser, T., Sandberg, J., Schoefer, V., Schultheiss, C., Seletskiy, S., Severino, F., Shrey, T., Smart, L., Smith, K., Song, H., Sukhanov, A., Than, R., Thieberger, P., Trabocchi, S., Tuozzolo, J., Wanderer, P., Wang, E., Wang, G., Weiss, D., Xiao, B., Xin, T., Xu, W., Zaltsman, A., Zhao, H., Zhao, Z.: Experimental demonstration of hadron beam cooling using radio-frequency accelerated electron bunches. Phys. Rev. Lett. **124**, 084801 (2020). https://doi.org/10.1103/PhysRevLett.124.084801
9. C. Krantz, H. Buhr, M. Grieser, M. Lestinsky, O. Novotný, S. Novotny, D.A. Orlov, R. Repnow, A.S. Terekhov, P. Wilhelm, A. Wolf, Transverse electron cooling of heavy molecular ions. Phys. Rev. Accel. Beams **24**(5), 050101 (2021). https://doi.org/10.1103/PhysRevAccelBeams.24.050101
10. D. Paul, M. Grieser, F. Grussie, R.v. Hahn, L.W. Isberner, A. K'alosi, C. Krantz, H. Kreckel, D. Müll, D.A. Neufeld, D.W. Savin, S. Schippers, P. Wilhelm, A. Wolf, M.G. Wolfire, O. Novotný, Experimental determination of the dissociative recombination rate coefficient for rotationally cold CH and its implications for diffuse cloud chemistry. Astrophys. J. **939**(2), 122 (2022). https://doi.org/10.3847/1538-4357/ac8e02
11. D. Gamba, F. Asvesta, P.M. Kruyt, L. Ponce, G. Russo, Status of e-cooling characterisation at 100 keV in ELENA, in *Proc. of the 14th Intl. Workshop on Beam Cooling and Related Topics (COOL2023)*, Vol. 40 (2023) https://doi.org/10.18429/JACoW-COOL2023-THPAM1R3
12. J.S. Bell, M. Bell, Electron cooling in storage rings. Part. Accel. **11**, 233 (1981). https://doi.org/10.1142/9789812795854_0002
13. H. Poth, Applications of electron cooling in atomic, nuclear and high-energy physics. Nature **345**, 399 (1990). https://doi.org/10.1038/345399a0
14. H. Danared, Electron cooling for atomic physics. Phys. Scr. **T59**, 121 (1995). https://doi.org/10.1088/0031-8949/1995/T59/014
15. G. Kilgus, D. Habs, D. Schwalm, A. Wolf, N.R. Badnell, A. Müller, High-resolution measurement of dielectronic recombination of lithiumlike Cu^{26+}. Phys. Rev. A **46**, 5730 (1992). https://doi.org/10.1103/PhysRevA.46.5730
16. A. Wolf, G. Gwinner, J. Linkemann, A.A. Saghiri, M. Schmitt, D. Schwalm, M. Grieser, M. Beutelspacher, T. Bartsch, C. Brandau, A. Hoffknecht, A. Müller, S. Schippers, O. Uwira, D.W. Savin, Recombination in electron coolers. Nucl. Instrum. Methods Phys. Res. Sect. A **441**, 183 (2000). https://doi.org/10.1016/S0168-9002(99)01131-6
17. M. Lestinsky, E. Lindroth, D.A. Orlov, E.W. Schmidt, S. Schippers, S. Bohm, C. Brandau, F. Sprenger, A.S. Terekhov, A. Müller, A. Wolf, Screened radiative corrections from hyperfine-split dielectronic resonances in lithiumlike scandium. Phys. Rev. Lett. **100**, 033001 (2008). https://doi.org/10.1103/PhysRevLett.100.033001
18. S. Schippers, Electron–ion merged-beam experiments at heavy-ion storage rings. Nucl. Instrum. Methods Phys. Res. Sect. B **350**, 61 (2015). https://doi.org/10.1016/j.nimb.2014.12.050

19. C. Krantz, N.R. Badnell, A. Müller, S. Schippers, A. Wolf, Recombination of open-f-shell tungsten ions. J. Phys. B At. Mol. Opt. Phys. **50**, 052001 (2017). https://doi.org/10.1088/1361-6455/aa547d
20. S. Schippers, C. Brandau, S. Fuchs, M. Lestinsky, S.X. Wang, C.Y. Zhang, N.R. Badnell, A. Borovik, M. Fogle, V. Hannen, Z. Harman, P.-M. Hillenbrand, E.B. Menz, Y. Zhang, Z. Andelkovic, F. Herfurth, R. Heß, A. Kalinin, C. Kozhuharov, C. Krantz, S. Litvinov, B. Lorentz, U. Spillmann, M. Steck, G. Vorobyev, D. Banaś, S. Fritzsche, E. Lindroth, X. Ma, A. Müller, R. Schuch, A. Surzhykov, M. Trassinelli, K. Ueberholz, C. Weinheimer, T. Stöhlker, Testing strong-field QED to second order in the highly correlated atomic system berylliumlike Pb by electron-ion collision spectroscopy. Phys. Rev. Lett. **135**, 113001 (2025). https://doi.org/10.1103/6j3v-lwxj
21. M. Lestinsky, V. Andrianov, B. Aurand, V. Bagnoud, D. Bernhardt, H. Beyer, S. Bishop, K. Blaum, A. Bleile, A. Borovik, F. Bosch, C.J. Bostock, C. Brandau, A. Bräuning-Demian, I. Bray, T. Davinson, B. Ebinger, A. Echler, P. Egelhof, A. Ehresmann, M. Engström, C. Enss, N. Ferreira, D. Fischer, A. Fleischmann, E. Förster, S. Fritzsche, R. Geithner, S. Geyer, J. Glorius, K. Göbel, O. Gorda, J. Goullon, P. Grabitz, R. Grisenti, A. Gumberidze, S. Hagmann, M. Heil, A. Heinz, F. Herfurth, R. Heß, P.-M. Hillenbrand, R. Hubele, P. Indelicato, A. Källberg, O. Kester, O. Kiselev, A. Knie, C. Kozhuharov, S. Kraft-Bermuth, T. Kühl, G. Lane, Y.A. Litvinov, D. Liesen, X.W. Ma, R. Märtin, R. Moshammer, A. Müller, S. Namba, P. Neumeyer, T. Nilsson, W. Nörtershäuser, G. Paulus, N. Petridis, M. Reed, R. Reifarth, P. Reiß, J. Rothhardt, R. Sanchez, M.S. Sanjari, S. Schippers, H.T. Schmidt, D. Schneider, P. Scholz, R. Schuch, M. Schulz, V. Shabaev, A. Simonsson, J. Sjöholm, O. Skeppstedt, K. Sonnabend, U. Spillmann, K. Stiebing, M. Steck, T. Stöhlker, A. Surzhykov, S. Torilov, E. Träbert, M. Trassinelli, S. Trotsenko, X.L. Tu, I. Uschmann, P.M. Walker, G. Weber, D.F.A. Winters, P.J. Woods, H.Y. Zhao, Y.H. Zhang, Physics book: CRYRING@ESR. Eur. Phys. J. Spec. Top. **225**, 797 (2016). https://doi.org/10.1140/epjst/e2016-02643-6
22. K. Abrahamsson, G. Andler, L. Bagge, E. Beebe, P. Carlé, H. Danared, S. Egnell, K. Ehrnstén, M. Engström, C.J. Herrlander, J. Hilke, J. Jeansson, A. Källberg, S. Leontein, L. Liljeby, A. Nilsson, A. Paal, K.-G. Rensfelt, U. Rosengård, A. Simonsson, A. Soltan, J. Starker, M. Ugglas, A. Filevich, CRYRING – a synchrotron, cooler and storage ring. Nucl. Instrum. Methods Phys. Res. Sect. B **79**, 269 (1993). https://doi.org/10.1016/0168-583X(93)95341-2
23. M. Lestinsky, E.B. Menz, H. Danared, C. Krantz, E. Lindroth, Z. Andelkovic, C. Brandau, A. Bräuning-Demian, S. Fedotova, W. Geithner, F. Herfurth, A. Kalinin, I. Kraus, U. Spillmann, G. Vorobyev, T. Stöhlker, First experiments with CRYRING@ESR. Atoms **10**, 141 (2022). https://doi.org/10.3390/atoms10040141
24. Krantz, C., Andelkovic, Z., Brandau, C., Dimopoulou, C., Geithner, W., Hackler, T., Hannen, V., Herfurth, F., Heß, R., Lestinsky, M., Menz, E., Reiter, A., Roßbach, J., Schippers, S., Schroeder, C., Täschner, A., Vorobjev, G., Weinheimer, C., Winzen, D.: Recommissioning of the CRYRING@ESR electron cooler, in *Proc. of the 12th Int. Part. Accel. Conf. (IPAC2021)*, Vol. 1816 (2021) https://doi.org/10.18429/JACoW-IPAC2021-TUPAB178
25. H. Danared, G. Andler, L. Bagge, C.J. Herrlander, J. Hilke, J. Jeansson, A. Källberg, A. Nilsson, A. Paál, K.-G. Rensfelt, U. Rosengård, J. Starker, M. Ugglas, Electron cooling with an ultracold electron beam. Phys. Rev. Lett. **72**, 3775 (1994). https://doi.org/10.1103/PhysRevLett.72.3775
26. H. Danared, A. Källberg, G. Andler, L. Bagge, F. Österdahl, A. Paál, K.G. Rensfelt, A. Simonsson, O. Skeppstedt, M. Af Ugglas, Studies of electron cooling with a highly expanded electron beam. Nucl. Instrum. Methods Phys. Res. Sect. A **441**, 123 (2000). https://doi.org/10.1016/S0168-9002(99)01121-3
27. D.A. Orlov, C. Krantz, A. Shornikov, M. Lestinsky, J. Hoffmann, A.S. Jaroshevich, S.N. Kosolobov, A.S. Terekhov, A. Wolf, Ultra cold photoelectron beams for ion storage rings. AIP Conf. Proc. **1149**, 1007 (2009). https://doi.org/10.1063/1.3215583
28. C. Brandau, S. Fuchs, V. Hannen, E.O. Hanu, C. Krantz, M. Lestinsky, M. Looshorn, E.B. Menz, S.X. Wang, S. Schippers, Electron-ion collision spectroscopy at the CRYRING@ESR electron cooler. Chin. Phys. C **49**, 064001 (2025). https://doi.org/10.1088/1674-1137/adbf81
29. S.-X. Wang, C. Brandau, S. Fritzsche, S. Fuchs, Z. Harman, C. Kozhuharov, A. Müller, M. Steck, S. Schippers, Breit interaction in dielectronic recombination of hydrogenlike xenon ions: storage-ring experiment and theory. Eur. Phys. J. D **78**, 122 (2024). https://doi.org/10.1140/epjd/s10053-024-00914-7
30. A. Müller, Plasma rate coefficients for highly charged ion–electron collisions: new experimental access via ion storage rings. Int. J. Mass Spectrom. **192**, 9 (1999). https://doi.org/10.1016/S1387-3806(99)00098-6
31. A. Hoffknecht, C. Brandau, T. Bartsch, C. Böhme, H. Knopp, S. Schippers, A. Müller, C. Kozhuharov, K. Beckert, F. Bosch, B. Franzke, A. Krämer, P.H. Mokler, F. Nolden, M. Steck, T. Stöhlker, Z. Stachura, Recombination of bare Bi $^{83+}$ ions with electrons. Phys. Rev. A **63**, 012702 (2000). https://doi.org/10.1103/PhysRevA.63.012702
32. A. Koutsostathis, C. Krantz, E.-O. Hanu, F. Herfurth, R. Heß, W. Kaufmann, M. Lestinsky, M.D. Looshorn, E.B. Menz, A. Reiter, J. Roßbach, S. Schippers, P.M. Suherman, Upgrades and maintenance of the CRYRING@ESR electron cooler for improved internal electron target operation. HNPS Adv. Nucl. Phys. **31**, 86 (2025). https://doi.org/10.12681/hnpsanp.7988
33. P. Glans, E. Lindroth, N. Eklo, M. Pajek, H. Danared, R. Schuch, Dielectronic recombination of Li-like fluorine ions. Nucl. Instrum. Methods Phys. Res. Sect. B **154**, 97 (1999). https://doi.org/10.1016/S0168-583X(99)00005-1
34. M. Tokman, N. Eklöw, P. Glans, E. Lindroth, R. Schuch, G. Gwinner, D. Schwalm, A. Wolf, A. Hoffknecht, A. Müller, S. Schippers, Dielectronic recombination resonances in F^{6+}. Phys. Rev. **66**, 012703 (2002). https://doi.org/10.1103/PhysRevA.66.012703
35. Lestinsky M. High-resolution electron collision spectroscopy with multicharged ions in merged beams. Dissertation, University of Heidelberg (2007). https://doi.org/10.11588/heidok.00007334

36. Krantz C. Intense electron beams from GaAs photocathodes as a tool for molecular and atomic physics. Dissertation, University of Heidelberg (2009). https://doi.org/10.11588/heidok.00010009
37. E. Lindroth, H. Danared, P. Glans, Z. Pešić, M. Tokman, G. Vikor, R. Schuch, QED effects in Cu-like Pb recombination resonances near threshold. Phys. Rev. Lett. **86**, 5027 (2001). https://doi.org/10.1103/PhysRevLett.86.5027